Advancing diffusion MRI: improving image quality and getting rid of the fat

Dong, Y.

Chapter 2

Regularized joint water/fat separation with B_0 map estimation in image space for 2D-navigated interleaved EPI based diffusion MRI

Yiming Dong, Kirsten Koolstra, Malte Riedel, Matthias J.P. van Osch, Peter Börnert

Magnetic Resonance in Medicine, 86(6), 3034-3051.

Abstract

Purpose: To develop a new water/fat separation and B_0 estimation algorithm to effectively suppress the multiple resonances of fat signal in echo planar imaging (EPI). This is especially relevant for diffusion-weighted (DW) imaging where fat is often a confounding factor.

Methods: Water/fat separation based on chemical-shift encoding enables robust fat suppression in routine MRI. However, for EPI the different chemical-shift displacements of the multiple fat resonances along the phase-encoding direction can be problematic for conventional separation algorithms. This work proposes a suitable model approximation for EPI under B_0 and fat off-resonance effects, providing a feasible multi-peak water/fat separation algorithm. Simulations were performed to validate the algorithm. In-vivo validation was performed in 6 volunteers, acquiring spin-echo EPI images in the leg (B_0 homogeneous) and head-neck (B_0 inhomogeneous) regions, using a TE-shifted interleaved EPI sequence with/without diffusion sensitization. The results are numerically and statistically compared with voxel-independent water/fat separation and fat saturation techniques to demonstrate the performance of the proposed algorithm.

Results: The reference separation algorithm without the proposed spatial shift correction caused water-fat ambiguities in simulations and in-vivo experiments. Some spectrally selective fat saturation approaches also failed to suppress fat in regions with severe B_0 inhomogeneities. The proposed algorithm was able to achieve improved fat suppression for DWI data and ADC maps in the head-neck and leg regions.

Conclusion: The proposed algorithm shows improved suppression of the multi-peak fat components in multi-shot interleaved EPI applications compared to the conventional fat saturation approaches and separation algorithms.

2.1 Introduction

Diffusion-weighted imaging (DWI), which is used to probe the thermal motion of water molecules, plays an important role in many clinical applications. This includes the diagnosis of tumors and stroke and the exploration of structural connectivity[1,2]. Single-shot EPI (ssh-EPI) readout is often preferred due to its high sampling efficiency and its ability to virtually freeze motion. However, ssh-EPI with its relatively small bandwidth along the phase-encoding direction is prone to geometric distortions caused by strong local B_0 inhomogeneities. Moreover, the long echo train may lead to substantial T_2* blurring, ultimately limiting the spatial resolution and the SNR. To mitigate the above-mentioned problems, multi-shot interleaved EPI (msh-EPI) has become a commonly used technique[3], which allows uniform k-space sampling by acquiring multiple interleaves for full k-space coverage. However, msh-EPI is particularly sensitive to subject motion when used for DWI. Motion can introduce significant phase inconsistencies between shots, thereby spoiling the overall coherence of the k-space data. Therefore, a low-resolution navigator can be added to probe and subsequently correct for physiological motion-induced phase alterations[4].

Beyond the brain, DWI can provide valuable information to characterize lesions and determine appropriate treatment strategies in body applications. DWI was reported to be successfully applied to diagnose and monitor the treatments of head and neck squamous cell carcinoma[5-7]. However, residual fat signals reduce the image quality and make improvements of the challenging fat suppression desirable. Although msh-EPI has an increased bandwidth in the phase-encoding direction compared to ssh-EPI, the fat signals (with the dominant CH_2 methylene proton peak at 1.3 ppm) still shift significantly with respect to water. When not suppressed, fat can obscure tiny structures in regions with overlapping water/fat signals. Furthermore, due to the multi-peak nature of the fat spectrum[8-10], the different lipid signals corresponding to the different chemical sites within the fat molecule are shifted to different locations. Conventional spectrally selective fat saturation methods such as SPIR/SPAIR[11,12] have been used to suppress fat signals before sampling. Nevertheless, such spectral selective techniques tend to fail in regions of high B_0 inhomogeneity, as encountered in the head-neck region[13-14]. Such failures can even result in an undesired suppression of the water signal, while leaving the fat untouched. The imperfect suppression will affect image quality in most EPI based applications, but especially in DWI[15], because remaining minor fat resonances can

still cause substantial ghosting at higher b-values due to their neglectable attenuation by diffusion compared to water[16-18].

As an alternative to fat saturation, water/fat separation approaches based on chemical-shift encoding using multiple TEs[19-21] gained growing popularity. Several approaches have been proposed to improve water/fat separation in EPI-based DWI. Burakiewicz et al. [22] proposed an approach to acquire DW images using a chemical-shift encoded spin-echo ssh-EPI sequence with an additional low-resolution navigator, assuming a single line fat spectrum and ignoring the ssh-EPI trajectory when disentangling water and fat. To deal with the multi-peak nature of the fat spectrum in DWI, previous works[17-18] attempted to correct for artifacts from those multiple fat peaks by combining fat saturation and chemical-shift encoding approaches. Recently, Hu et al. [23] presented an alternative msh-EPI approach to remove the fat signals in DWI by using the PSF-EPI approach adding an additional encoding dimension to encode chemical-shift.

In this study, a simpler approach is proposed using a navigator-based DW msh-EPI approach (IRIS, "image reconstruction using image-space sampling function")[4] extended by chemical-shift encoding to suppress the fat. After reconstruction of the chemical-shift encoded multi-shot images, a new regularized water/fat separation algorithm is applied, which was adapted to the EPI sampling process. This algorithm is working in the image domain addressing the chemical-shift displacements of fat in the phase-encoding direction. This was done using a series of shift matrices, applied to the common B_0 field map, in the joint estimation of B_0, water and all fat components. This work is mainly focused on improving image quality for the water images, to especially support diffusion applications. Thus, chemical-shift encoding is applied for fat suppression, not risking touching the water magnetization by any magnetization preparation. The algorithm was tested in simulations, providing a ground truth for numerical/statistical comparison, and on healthy volunteer data acquired with a TE-shifted spin-echo msh-EPI with and without diffusion encoding. For comparison, a voxel-independent iterative decomposition of water and fat with echo asymmetry and least-squares (IDEAL)[21] algorithm and conventional fat saturation techniques were applied. Numerical/statistical analyses were performed among the three different techniques.

2.2 METHODS

Sequence

To enable water/fat chemical-shift encoding, the 2D-navigated DW msh-EPI approach[4] was complemented by adding appropriate image echo shift functionality[22] as shown in figure 1. For a given b-value, a series of chemical-shift encoded (e.g. N = 3) source data can be acquired, changing slightly the timing of the msh-EPI train while keeping the timing of the low-resolution phase navigator fixed.

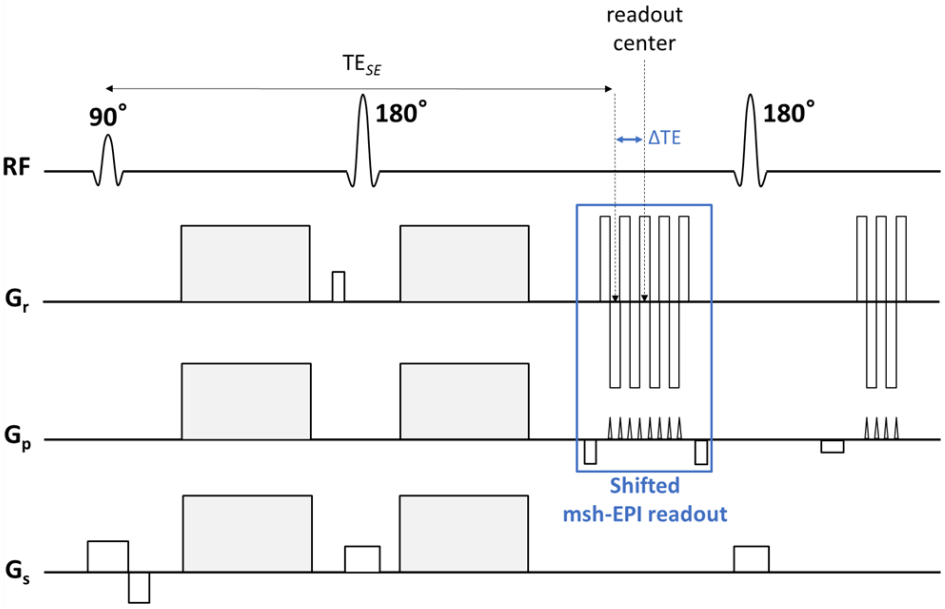

Figure 1. Scheme of the used segmented diffusion EPI sequence allowing for water/fat chemical-shift encoding and navigator correction. The msh-EPI sampling window can be shifted back and forth by a time interval (ΔTE) relative to the time of the spin echo (TE$_{SE}$) to facilitate chemical-shift encoding. Please note that the timing of the navigator echo remains fixed to sense potential phase distortions, introduced due to physiological motion during the diffusion sensitizing process. The gray colored gradients, applied on all channels simultaneously, are used for diffusion sensitization.

To avoid phase discontinuities due to off-resonance effects among the individual segments of the basic msh-EPI acquisition, time shifting[24] is applied using a shift increment τ (duration of one EPI read-out lobe divided by the segmentation factor). This time base is also used to facilitate chemical-shift encoding by shifting the msh-EPI block by integer multiples of τ, for simplicity reasons.

Signal model

Due to the low bandwidth in the phase-encoding direction in EPI, the displacement of fat in this direction can be extremely large. For a given voxel in an EPI image that contains both water and fat, the fat portion is shifted and originates from another voxel/location than the water signal. Therefore, the fat signal in a voxel will also have experienced a different B_0 inhomogeneity compared to the water reconstructed within the same voxel[17]. The multi-peak nature of fat poses extra challenges. Each fat peak has a different spatial shift and therefore has experienced a different B_0 inhomogeneity compared to the other fat signals reconstructed in the same voxel; moreover, each fat peak will appear with a different amplitude in the image[8-10,17]. Thus, the total signal model of one voxel can be written as:

$$S_n\big(w(x,y), f(x,y), \varphi_B(x,y)\big) =$$

$$w(x,y)e^{i2\pi\varphi_B(x,y)\Delta\mathrm{TE}_n} + \sum_{m=1}^{M} \alpha_m f(x, y+\Delta y_m) e^{i2\pi\varphi_B(x,y+\Delta y_m)\Delta\mathrm{TE}_n} e^{i2\pi\varphi_{F,m}\Delta\mathrm{TE}_n} + v_n(x,y) \quad (1)$$

where w and f denote the complex-valued water and fat components, $\Delta\mathrm{TE}_n$ [s] the time shift between the readout center of the n-th TE-shifted scan and the spin echo TE_{SE} [s], φ_B [Hz] the B_0 map at the original (x,y) and shifted $(x, y+\Delta y_m)$ location. Furthermore, α_m and $\varphi_{F,m}$ [Hz] give the relative amplitude and chemical-shift for each fat peak m, whereas v_n denotes the complex noise. Please note, this signal model is a simplification, it is addressing the fat shift effects in phase encoding direction, but neglects the small chemical-shift effects in the (odd/even) readout direction with the aim to yield a feasible solution for EPI in image-space.

Algorithm

In this work, a two-step approach is chosen, as in the voxel-independent IDEAL algorithm[21], to solve Eq. (1) for w, f and B_0: (I) a water/fat separation step, followed by (II) a field map estimation step, is performed in an iterative process. Unless stated otherwise, the initial B_0 field map is set to $\Phi_B = 0$ for the first iteration of (I). After the incremental error $\Delta\Phi_B$ is calculated using the Gauss-Newton approach in (II), we update $\Phi_B = \Phi_B + \Delta\Phi_B$ and repeat steps (I) and (II) until the number of iterations reaches the threshold (often ≤ 10 iterations). Due to the low phase encoding bandwidth of EPI, established approaches that ignore spatial shifts[21,25-26] are no longer suitable to estimate individual water/fat contents and the B_0 inhomogeneity induced phase in every voxel[17-18]. Therefore, a joint estimation algorithm is

implemented that considers the spatial shift both for the B_0 map and for the individual fat peaks. These spatial shifts are implemented via shift matrices.

I. Water/fat separation

Equation 1 can be discretized and written as

$$S = \hat{A}X, \tag{2}$$

where S and X are vectorized representations of the N source images and the unknown water/fat components, respectively, i.e.

$$S = \left[s_1^1, \dots, s_1^Q, \dots, s_N^1, \dots, s_N^Q\right]^T \tag{3}$$

and

$$X = [W, F]^T = [w^1, \dots, w^Q, f^1, \dots, f^Q]^T, \tag{4}$$

where Q is the number of voxels. Then, Eq. 2 is written into the minimization problem

$$\bar{X} = \underset{X \in \mathbb{C}^{2Q}}{\operatorname{argmin}} \left\|\hat{A}X - S\right\|_2^2. \tag{5}$$

$\hat{A}$ is the coefficient matrix

$$\hat{A} = \begin{bmatrix} A_{11} & A_{12} \\ \vdots & \vdots \\ A_{N1} & A_{N2} \end{bmatrix}, \tag{6}$$

with

$$A_{n1} = diag\left(e^{i2\pi\varphi_B^1 \Delta \mathrm{TE}_n}, \dots, e^{i2\pi\varphi_B^Q \Delta \mathrm{TE}_n}\right), \tag{7}$$

$$A_{n2} = \sum_{m=1}^{M} \alpha_m diag\left(e^{i2\pi\varphi_{B,m}^1 \Delta \mathrm{TE}_n} e^{i2\pi\varphi_{F,m} \Delta \mathrm{TE}_n}, \dots, e^{i2\pi\varphi_{B,m}^Q \Delta \mathrm{TE}_n} e^{i2\pi\varphi_{F,m} \Delta \mathrm{TE}_n}\right) L_m \tag{8}$$

and φ_B^q the B_0 field at voxel q, such that

$$\Phi_B = \left[\varphi_B^1, \dots, \varphi_B^Q\right]^T. \tag{9}$$

For each fat peak m, a shifted version of the field map, $\Phi_{B,m}$, can be written as

$$\Phi_{B,m} = \left[\varphi_{B,m}^1, \dots, \varphi_{B,m}^Q\right]^T = L_m \Phi_B, \tag{10}$$

where L_m is a shift matrix that spatially shifts the whole fat image l_m voxels in the phase-encoding direction. Similar to the image-domain approach in[15], the spatial displacement l_m can only take integer numbers. The voxel shift l_m for each fat peak m can be calculated from

$$l_m = \left[\frac{\varphi_{F,m}}{BW}\right], \tag{11}$$

where BW is the bandwidth in phase-encoding direction [Hz/pixel] and $[\cdot]$ denotes rounding to the nearest integer.

Finally, Eq. 5 is written into the linear least squares system

$$\hat{A}^H \hat{A} X = \hat{A}^H S \tag{12}$$

and solved with the Conjugate Gradient (CG) method.

II. Field map estimation

The field map estimation is based on a Gauss–Newton search method. Similar to (21), the error terms of each unknown are introduced by writing $w(x,y)$, $f(x,y)$, and $\varphi_B(x,y)$ in Eq.(1) as $w(x,y) + \Delta w(x,y)$, $f(x,y) + \Delta f(x,y)$, and $\varphi_B(x,y) + \Delta\varphi_B(x,y)$ and neglecting second-order error terms. Using the first-order Taylor expansion of $\Delta\varphi_B$ yields:

$$S_n\big(w(x,y), f(x,y), \varphi_B(x,y)\big)$$

$$= w(x,y)e^{i2\pi\varphi_B(x,y)\Delta\mathrm{TE}_n} + \sum_{m=1}^{M} \alpha_m f(x, y+\Delta y_m) e^{i2\pi\varphi_B(x,y+\Delta y_m)\Delta\mathrm{TE}_n} e^{i2\pi\varphi_{F,m}\Delta\mathrm{TE}_n}$$

$$+\Delta w(x,y)e^{i2\pi\varphi_B(x,y)\Delta\mathrm{TE}_n}$$

$$+ \sum_{m=1}^{M} \alpha_m \Delta f(x, y+\Delta y_m) e^{i2\pi\varphi_B(x,y+\Delta y_m)\Delta\mathrm{TE}_n} e^{i2\pi\varphi_{F,m}\Delta\mathrm{TE}_n}$$

$$+i2\pi\Delta\mathrm{TE}_n\Delta\varphi_B(x,y)w(x,y)e^{i2\pi\varphi_B(x,y)\Delta\mathrm{TE}_n}$$

$$+\sum_{m=1}^{M} i2\pi\Delta\mathrm{TE}_n\Delta\varphi_B(x,y+\Delta y_m)\alpha_m f(x,y+\Delta y_m)e^{i2\pi\varphi_B(x,y+\Delta y_m)\Delta\mathrm{TE}_n}e^{i2\pi\varphi_{F,m}\Delta\mathrm{TE}_n}$$

$$+v_n(x,y). \tag{13}$$

Eq. 13 can be discretized and written into the minimization problem:

$$\{\Delta\bar{\Phi}_B,\Delta\bar{W},\Delta\bar{F}\}=\underset{\substack{\Delta\Phi_B\in\mathbb{R}^Q\\ \Delta W,\Delta F\in\mathbb{C}^Q}}{\operatorname{argmin}}\left\|\Delta S-\hat{B}\Delta Y\right\|_2^2+\lambda TV(\Delta\Phi_B), \tag{14}$$

where

$$\Delta S=S-\hat{A}\bar{X}, \tag{15}$$

$$\Delta Y=[\Delta W,\Delta F,\Delta\Phi_B]^T=\left[\Delta w^1,\dots,\Delta w^Q,\Delta f^1,\dots,\Delta f^Q,\Delta\varphi_B^1,\dots,\Delta\varphi_B^Q\right]^T, \tag{16}$$

and ΔW, ΔF and $\Delta\Phi_B$ are errors of the unknowns W, F and Φ_B. $\bar{X}$ is the current estimation obtained from solving Eq.12. In each iteration, the error map $\Delta\bar{\Phi}_B$ is calculated corresponding to the estimated B_0 map Φ_B and updated to $\Phi_B=\Delta\bar{\Phi}_B+\Phi_B$. TV is the well-known total variation regularization operator, that can be used to enforce smoothness[27-29] of the updated field map error. Specifically,

$$TV(\Delta\Phi_B)=\left\|\nabla_x(\Delta\Phi_B)\right\|_2^2+\left\|\nabla_y(\Delta\Phi_B)\right\|_2^2 \tag{17}$$

where ∇_x and ∇_y are backward first derivative operators for x and y directions, respectively. Furthermore, λ in Eq.14 is the regularization factor that weights the smoothness of the field map and is tuned empirically. The coefficient matrix $\hat{B}$ can easily be built by using the block matrix elements directly from matrix $\hat{A}$, i.e.,

$$\hat{B}=\begin{bmatrix}A_{11} & A_{12} & B_1\\ \vdots & \vdots & \vdots\\ A_{N1} & A_{N2} & B_{N2}\end{bmatrix}, \tag{18}$$

where

$$B_n = i2\pi\Delta\mathrm{TE}_n A_{n1} W + \sum_{m=1}^{M} i2\pi\Delta\mathrm{TE}_n \left(A_{n2,m} F\right) L_m \,. \tag{19}$$

Then, the error $\Delta\Phi_B$ for updating the field map can be calculated by solving

$$\hat{B}^H \Delta S = \left(\hat{B}^H \hat{B} + \lambda \hat{D}_x^H \hat{D}_x + \lambda \hat{D}_y^H \hat{D}_y\right) \Delta Y \tag{20}$$

with CG, using

$$\hat{D}_{\substack{x \\ y}} = \begin{bmatrix} 0 & 0 & 0 \\ 0 & 0 & 0 \\ 0 & 0 & \nabla_{\substack{x \\ y}} \end{bmatrix}. \tag{21}$$

Since the B_0 values are treated as real values in the current implementation, the complex vectors $\Delta W, \Delta F$ and ΔS are split into real and imaginary parts according to (21) as well as all the corresponding matrix elements.

B_0 map extrapolation

Due to the large displacement of fat, estimation of the local B_0 experienced by a fat component can be compromised at locations where fat is shifted outside the boundaries of the subject. Thus, an additional extrapolation step was implemented after a few iterations of the algorithm to produce a more stable B_0 reinitialization for the remaining iterations. The extrapolation step assumes that the inner area of the object has been shimmed well and is free from large inhomogeneities[30]. This is similar to the region-growing IDEAL approach[26], which is initialized by an automatically selected center-of-mass seed voxel. In the present approach, a thin-plate spline extrapolation method similar to ref.[31] is applied. An example of this approach can be found in Supporting Information Figure S1. Alternatively, the estimated field map from other methods[25-26,30,32-33] would also provide a reasonable initialization (although without consideration of the chemical-shift effects)[17].

Experiments

Simulation study

Shepp-Logan water/fat phantom data were simulated in k-space to generate sets of three chemical-shift encoded source images. One simulated B_0 map and the chemical-shift of each

fat peak were both modulated for each k-space data point with the actual sampling time, including time variations in both phase-encoding/readout directions. The sampling time map was generated based on the chosen phase-encoding bandwidth [Hz/pixel] and segmentation factors. Using a 3-point Dixon, the encoding steps were uniformly distributed over the full encoding circle, matching the dephasing period between methylene peak and water, which corresponds to 2.3 ms at 3T (ΔTEs = 0.24 ms, 1.00 ms, 1.76 ms). The signal-to-noise ratio was set to be 100, calculated as the maximal water signal intensities divided by the standard deviation of the noise. Using those data, water/fat separation was performed with the proposed algorithm using 10 iterations.

A voxel-independent multi-peak IDEAL algorithm implemented based on Refs. (21,34), using a median filter to smooth the estimated B_0 map, was applied for comparison. The maximum number of iterations of the IDEAL algorithm was set to 30. This basic voxel-independent algorithm was used as one of the reference methods, because it works also in image space, and represents the basic approach for water/fat separation (21). For simplicity, we will refer to this voxel-independent multi-peak IDEAL algorithm as IDEAL in all figures.

Numerical simulations were conducted to explore the effect of spatial integer shifts using varying bandwidths from 15 to 50 Hz/pixel (step size, 0.5 Hz/pixel), at a fixed relatively homogeneous B_0 field (2D Gaussian profile ranging from -110 to 110 Hz), a segmentation factor of 6 and a 7-peak fat model (10).

Two ROIs were defined, in a mixed region (water/fat overlap) and in a water-only pure region (no overlap). Overlapping and non-overlapping regions can be identified by taking the ground truth water/fat distribution, the given EPI bandwidth in the phase encoding direction and the chemical shift of each individual fat peak into account. It should be noticed that, due to the presence of B_0-introduced geometric distortions, the ground-truth images were also modulated with the same B_0 and time maps at each given bandwidth.

To reduce the potential “integer shift” discretization error, a simple zero-filling interpolation (ZIP) algorithm[35] was implemented. When the shift between water and the dominating fat resonance (methylene peak) corresponds to a fraction as half a pixel (half-pixel shift), the resulting mismatch due to the “integer shift” character of the image-domain algorithm, can be mitigated by interpolating the source images to a larger matrix. The separated water images of adopting the ZIP approach are shown in Supporting Information Figure S.2. In this simple

validation, the half-pixel effects of all the minor peaks, which have relatively lower amplitude, were not considered.

The normalized Root Mean Squared Error (NRMSE) between separated water image and the known ground truth water image were calculated through

$NRMSE = (\sqrt{\sum_{q=1}^{Q}(\hat{w}_q - w_q)^2/Q})/\bar{w}_q$, where $\hat{w}_q$ represents the ground truth water, w_q the separated water signal, $\bar{w}_q$ its average amplitudes and Q the number of voxels in the water image.

In-vivo volunteer study

Experiments were performed involving 8 healthy volunteers with informed consent obtained and approved by the local ethics committee. Interleaved multi-slice diffusion weighted EPI imaging was performed in the leg and the head/neck regions on a 3T scanner (Philips, Best, The Netherlands), using an 8-channel knee and a 16-channel head-neck array receive coil, respectively. Two basic protocols were applied comprising three b-values (0, 300, 600 s/mm^2) with all three gradients active in parallel, measuring four slices with a gap of 10 mm at a fixed TR of 2s. Thus, a single diffusion direction was used for DWI. For each b-value, three TE-shifted source images were acquired. Ramp sampling was used for all measurements and already corrected in the scanner reconstruction. Conventional fat saturation techniques were performed for comparison. In the leg experiments, 6 volunteers were measured with SPIR[11] and 2 were measured with SPAIR[12]. In the head-neck experiments only SPIR was applied. The main distinction between SPIR and SPAIR is the use of different RF pulses. By using an adiabatic inversion pulse, SPAIR has a better ability to cope with B_1^+ inhomogeneities, at the penalty of increased measuring time or reduced number of slices. The other sequence parameters are reported in Table 1.

DWI image reconstruction for the individual ΔTEs and b-values was performed off-line using a Python implementation of the IRIS algorithm[4]. The physiological motion induced phase distortions were sensed by the low-resolution navigator for each individual shot and were corrected by the IRIS algorithm, producing complex-valued chemical-shift encoded source images. No further interpolation of the three source images was performed (ZIP), because at the given EPI bandwidths the fraction of the methylene peak pixel shift was below ± 0.15 pixels. The coil sensitivity maps were pre-acquired using gradient echo imaging[36-37]. Thus,

they do not match exactly the distortions as encountered in the EPI and navigator images due to chemical-shift and B_0 displacements. Ignoring this mismatch during SENSE reconstruction will result in some residual unfolding and/or ghosting artifacts, even under smooth conditions. In the present work, a simple extrapolation of the coil-sensitivity maps is used to get a rough sensitivity estimate in areas where the pre-scan has seen no signal but the EPI did (see Supporting Information Figure S.3 for more details).

To improve convergence of the water/fat separation for each slice, the B_0 map obtained from b = 0 s/mm^2, was chosen as an initialization for the water/fat separation for higher b-values. This helped to reduce the number of iterations. Therefore, for the in-vivo data, the number of iterations was chosen to be 10 for b = 0 s/mm^2 data and 5 for higher b-values. The regularization factor λ was empirically chosen to be 1 for simulations, and 10^4 for in-vivo data. The threshold of the normalized residual norm for convergence of CG was set to 0.001 both for the water/fat separation step and the field map estimation step. The computational time per iteration was 1.5/9.9 seconds for a single-peak/multi-peak fat model in the simulation data (single slice, matrix size 144 x 144), and 17.4/21.6 seconds for a multi-peak fat model and medium/higher resolution in-vivo data (single slice, matrix size 150 x 160 / 162 x 168). All computations were performed on a Windows 10 computer with an Intel Core i7 CPU (3.0 GHz, 8 cores) and 32 GB of RAM.

Due to the lack of ground truth for the in-vivo data, numerical/statistical analyses were conducted by evaluating the apparent diffusion coefficient (ADC) fitting. Two ROIs were manually selected as pure water (no water/fat overlap) and mixed (overlap) regions. 200 pixels of each ROI were selected within the same muscle for each slice. Paired T-tests were performed between the fitted ADC values of each ROI, comparing the proposed algorithm with IDEAL and SPIR in 6 volunteers. A P-value < 0.05 indicated statistical significance.

Fat spectrum self-calibration

To achieve optimal water/fat separation, a correct fat spectrum model is essential. However, due to T_2 relaxation[8,10] and potential J-coupling[38-39] effects, Ren's spectral fat model[10] becomes inaccurate for the TE range used in this work. Therefore, a relative amplitude calibration was performed in a process like the one described in ref.[34], taking the fat resonance frequencies as known priors[10].

In this approach, self-calibration for the individual fat peaks was done sequentially due to the limited number of TEs. It was assumed that the calibration for each fat peak was not affected by the other peaks. The peaks were sorted and calibrated in descending order according to their weights in Ren's model. To do calibration for each peak separately, peak-specific fat masks were constructed in a subcutaneous fat only region of one volunteer's leg. Data for b=0 s/mm^2 were used, neglecting the small water content in fatty tissue[34]. After its definition, this fat mask was shifted along the phase-encoding direction by the corresponding number of pixels, determined by the peak's resonance frequency according to Eq. 11. To avoid potential biases from restricting shifts to integer steps, an additional boundary erosion step with one iteration was performed for each mask, assuring that all pixels inside the mask contain the fat signals of the calibrated peak. The methylene peak was set as the reference fat peak since it is supposed to be the most abundant component in the spectrum. Calibration started with the second peak, combined with the main peak to form a "temporary" two-peak fat model. Then, the proposed algorithm was performed while minimizing the residual fat signal leaking into the water channel as a function of the peak's amplitude. This process was repeated peak by peak until all peaks were included.

The final fat model obtained was $\varphi_{F,m}$ = [-485.41, -434.32, -397.27, -341.07, -312.96, -246.54, 77.92] Hz with normalized weights α_m = [0.067, 0.797, 0.000, 0.057, 0.010, 0.009, 0.059] (Original Ren's 7-peak fat model[10] weights: [0.085 , 0.625 , 0.071, 0.095, 0.066, 0.016, 0.042]) and was used for all other in-vivo reconstructions. The reduced relative amplitude of the fat peaks at -341.07, -312.96, and -246.54 Hz at a given TE may be due to their shorter T_2 compared to the remaining peaks (-485.41, -434.32, and 77.92 Hz)[8,10] or due to J-coupling effects[38-39]. Zero amplitude was found for the peak at -397.27 Hz, probably due to the difficulty to distinguish it from the dominant methylene peak[8]. The performance of the proposed algorithm with different numbers of peaks in the fat model is shown in Supporting Information Figure S.4.

Table 1. Sequence parameters for data acquisition.

anatomy	resolution (mm^3)	matrix size	seg. factor[a]	TE (ms)	ΔTE (ms)	bandwidth[b] (Hz/pixel)	Fat sat.	acquisition time (s)
leg	1.4 x 1.5 x 4	160 × 150	6	59	-	36.2	SPIR	51
	1.2 x 1.2 x 4	168 × 162	6	64	-	29.2	SPIR	51
	1.4 x 1.5 x 4	160 × 150	6	59	0.26 / 1.00 / 1.74	36.2	-	152
	1.2 x 1.2 x 4	168 × 162	6	64	0.26 / 1.00 / 1.74	29.2	-	152
	1.4 x 1.5 x 4	160 × 150	6	59	0.26 / 1.00 / 1.74	36.2	SPAIR	152
	1.2 x 1.2 x 4	168 × 162	6	64	0.26 / 1.00 / 1.74	29.2	SPAIR	152
head-neck	1.4 x 1.5 x 4	160 × 150	6	59	-	36.2	SPIR	51
	1.4 x 1.5 x 4	160 × 150	6	59	0.26 / 1.00 / 1.74	36.2	-	152
	1.4 x 1.5 x 4	160 × 152	8	53	-	47.5	SPIR	67
	1.4 x 1.5 x 4	160 × 152	8	53	0.16 / 1.00 / 1.84	47.5	-	200

[a]seg.factor: the segmentation factor
[b]bandwidth: the EPI bandwidth in phase-encoding direction

2.3 RESULTS

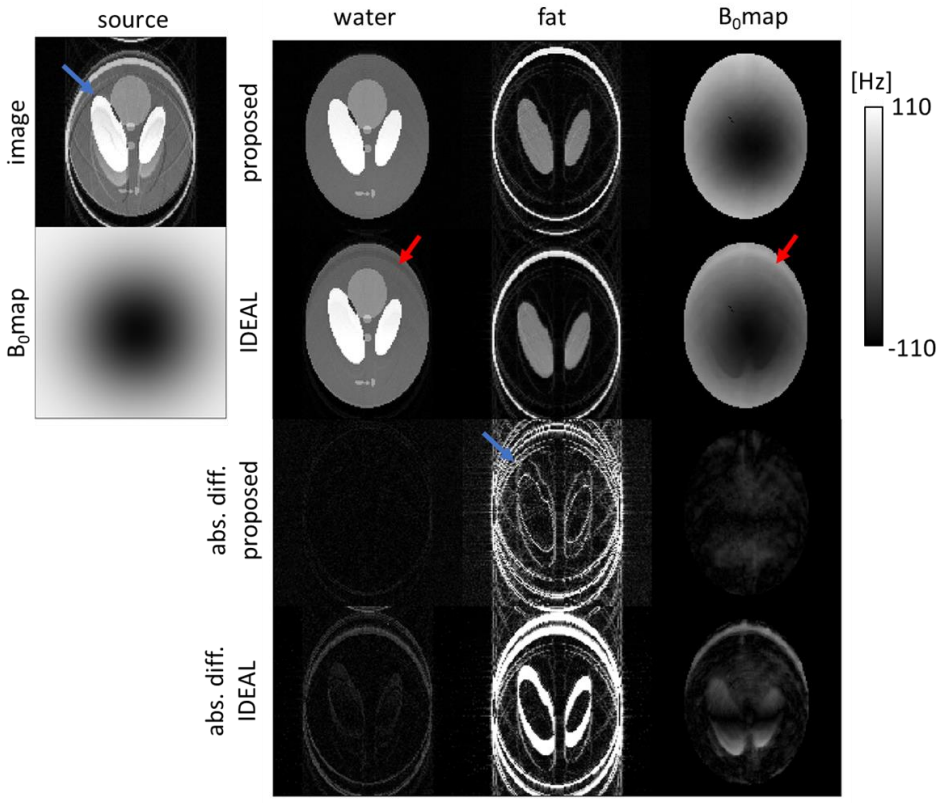

Figure 2. Interleaved EPI water/fat separation using simulation example data. One selected interleaved 6-shots EPI source image (bandwidth of 36 Hz/pixel), simulated with a B_0 map (range -110 to 110 Hz) and a 7-peak fat model. Estimated water, fat and B_0 maps from the proposed and the IDEAL algorithms are shown. For IDEAL, the omission of spatial shifts results in inaccurate B_0 map estimation and insufficient water/fat separation (marked by red arrows), whereas the proposed algorithm shows no distinct artifacts in the water image and B_0 map. Furthermore, the absolute difference maps (displayed with 5 times magnified scale) show improved accuracy for the proposed algorithm especially in water image and B_0 estimation compared to IDEAL. However, due to the simplification of the EPI signal model, for fat the errors in the fat image are larger than those for water (marked by the blue arrow).

Figure 2 shows water/fat separation results of phantom data sets using IDEAL and the proposed algorithm. The proposed algorithm produces good water images and B_0 estimations in the simulation. Though a benign B_0 map is simulated, IDEAL shows artifacts in the water and the B_0 channel mainly due to the neglection of spatial shifts of fat and the B_0 map.

Figure 3 shows the NRMSE plots of the simulation. The NRMSEs of the proposed algorithm are maintained at reasonable values close to the noise level (~0.019) in both regions. However, a slight oscillation in the error train can be seen for both mixed and pure ROIs. The maximum error amplitude always appears at those bandwidths where the dominant fat (methylene) peak is shifted to a “half pixel”. To mitigate errors resulting from the half-pixel

shift effects, interpolation of the image to a larger matrix size was proposed to ensure an "integer shift" for the methylene peak; this indeed did reduce the enhanced NRMSE (see Supporting Information Figure S.2).

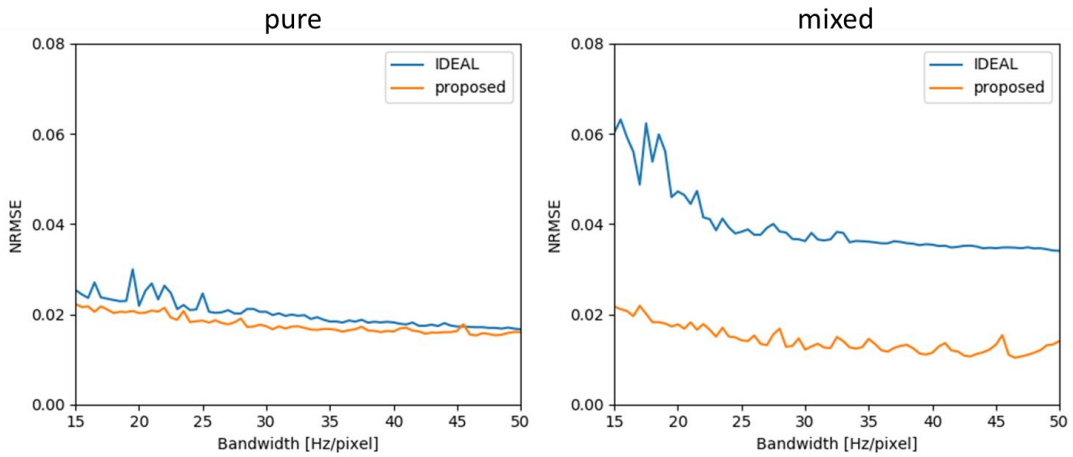

Figure 3. Normalized Root Mean Squared errors (NRMSE) for the water images as a function of the EPI bandwidth obtained in simulations. NRMSE between separated water and ground truth water image shown for mixed/pure ROIs, respectively. The source data is simulated with a 7-peak fat spectrum model and varying bandwidth. NRMSE in both regions of the proposed algorithm always remains around the noise level, whereas a slight error increase can be seen at bandwidths where the methylene peak is almost shifted to a "half pixel" (e.g., at 45.5 Hz/pixel). In comparison, IDEAL shows larger errors, especially in the mixed ROI.

Figure 4 shows decomposed water and fat images of one subject's leg and one subject's head-neck for both IDEAL and the proposed algorithm for a non-diffusion case. Neglecting the spatial shifts in the signal model, IDEAL results in an inaccurate water/fat decomposition. Moreover, in the head-neck slice, water/fat swap artifacts appears in regions of severe B_0 inhomogeneities. The proposed algorithm produces significantly improved results in both cases.

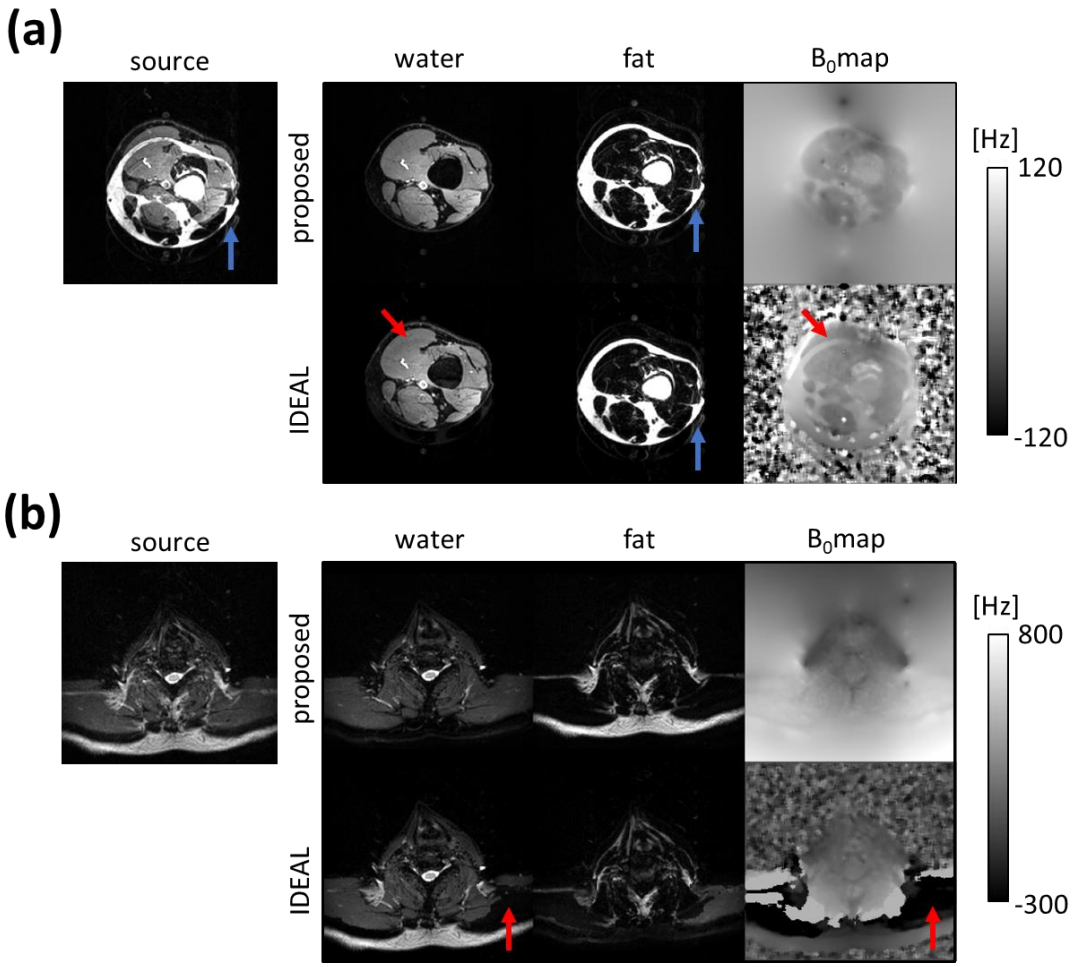

Figure 4. Comparison between the IDEAL and the proposed algorithm for non-diffusion sensitized (b = 0 s/mm^2) leg and head-neck data. (a) One source image of the reconstructed leg data and corresponding water/fat separation results from the proposed and IDEAL algorithms**.** IDEAL leaves rim-like artifacts (marked by red arrows) in the fat overlapping region in the B_0 map and water image. This artifact is not present when reconstructed with the proposed approach. Furthermore, some residual fat ghosting can be seen in both the source and the separated fat images of both algorithms due to the neglected chemical-shift effects in readout direction (indicated by the blue arrow). (b) One source image from the head-neck region and the water/fat separation results calculated through the proposed and voxel-independent algorithms. Significant errors in B_0 estimation cause artifacts in the corresponding regions of the water image for the IDEAL algorithm (marked by red arrows). With the help of the TV regularization and extrapolation used in the proposed algorithm, the B_0 errors and species swaps in the water/fat images from severe B_0 deviations appearing in the results of the IDEAL algorithms are reduced.

Figure 5 shows four slices of two subject's legs at b = 0 and 300 s/mm^2, comparing the proposed, voxel-independent IDEAL, and fat saturation method. The proposed algorithm provides more reliable water images in all slices for non-diffusion and diffusion cases in contrast to IDEAL. For SPIR (volunteer 1), although B_0 is rather homogeneous in the leg region, the B_1^+ inhomogeneity of the body coil transmission is another compromising factor (40-41), contributing to incomplete fat suppression (marked by the blue arrow) due to wave

propagation effects, which is not the case for SPAIR (volunteer 2). The image quality matches well between the proposed method and SPAIR especially regarding the methylene peak, while the fat signal contributed from the olefinic peak (5.31 ppm) can be further removed through the proposed approach (marked by the white arrows).

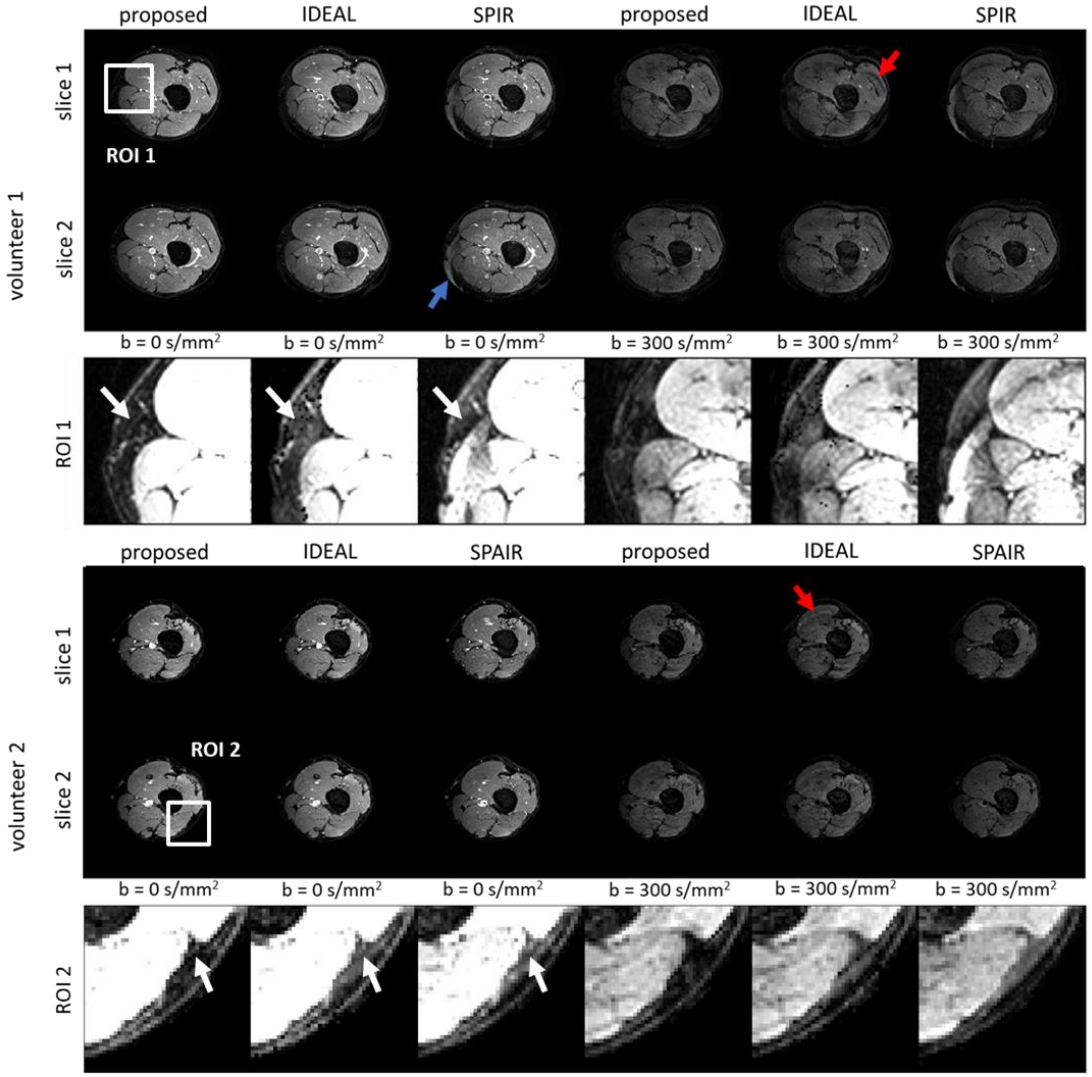

Figure 5. Comparison of three different approaches in two subject's legs. Four slices of water-only images selected from two volunteers at two b-values are shown. For the fat saturation data, SPIR and SPAIR were applied in volunteer 1 and 2, respectively. The proposed algorithm produces good water/fat decompositions both with and without diffusion gradients. The fat-related artifacts as shown in Figure 4 appear in the IDEAL images as well (marked by red arrows). For SPIR in volunteer 1, an artifact resulting from B_1^+ inhomogeneity can be seen (marked by the blue arrow). In volunteer 2, SPAIR avoids this artifact. Two ROIs are selected (marked by the white squares) and used for all approaches, illustrated at the bottom with adjusted level/window. With the help of shift matrices, the fat components from different fat peaks can be suppressed simultaneously, whereas other methods show residual fat signals in the water-only images (e.g., olefinic peak, marked by the white arrows).

Figure 6 shows results of one subject's head-neck DWI at two b-values comparing SPIR, IDEAL, and the proposed method. SPIR and IDEAL suffer from large field inhomogeneities in the outer image areas due to bad B_0 shimming conditions, showing remaining artifacts in the water-only images. The proposed algorithm can resolve the ambiguities from chemical-shifted fat and produce better water/fat separation.

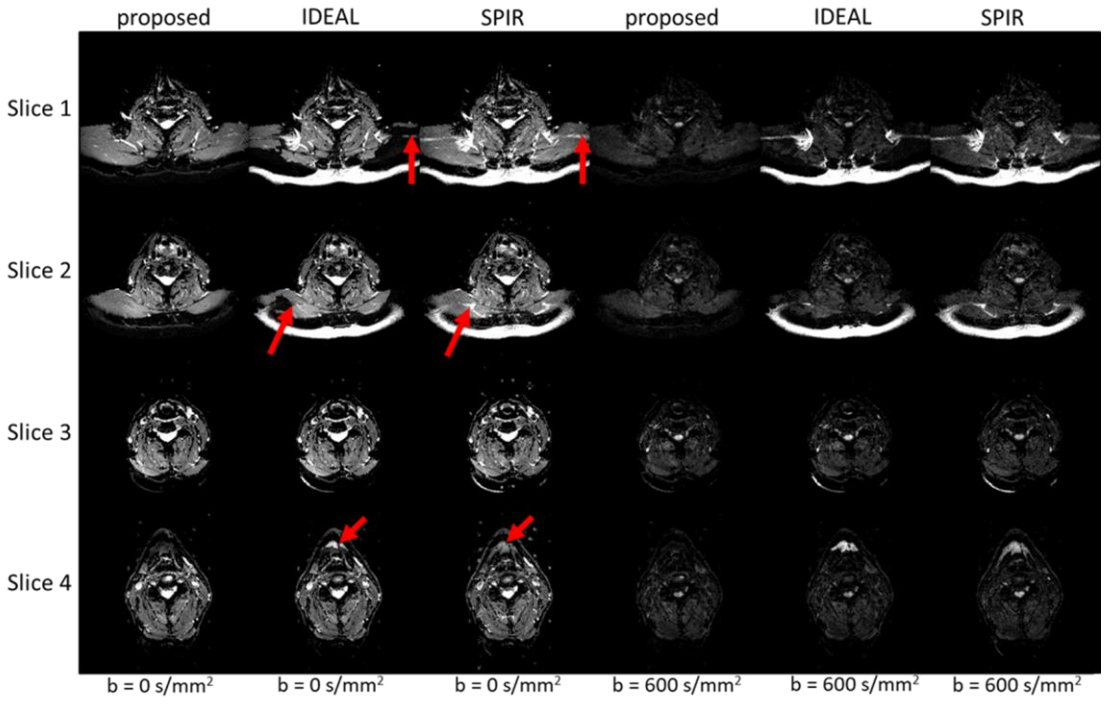

Figure 6. Comparison of the three different approaches in one subject's head-neck region. Four slices with two b-values are displayed. Due to the severe field inhomogeneities in this case, the fat signal can neither be completely suppressed by SPIR, nor separated by IDEAL (marked by the red arrows). The proposed algorithm produces significantly improved water/fat separation, especially in regions where IDEAL generates water/fat swaps.

Figure 7 shows two example ADC maps for the three fat suppression techniques both for the leg and for the head-neck data. The proposed algorithm produces better ADC quantifications in both anatomies, compared to IDEAL and SPIR with the previously described artifacts.

Figure 8 shows the natural logarithm of the water signal intensities varying as a function of the b-values. In the leg anatomies (a), IDEAL shows inconsistent log-signal decays between the two chosen ROIs. The proposed algorithm and SPIR adhere more to the expected linear decrease in the logarithmic plots although SPIR was slightly affected by B_1^+ inhomogeneities (marked by the blue arrow in Figure 7). In the head-neck regions (b), the critical B_0 inhomogeneities contribute to species swap in the IDEAL water images and incomplete fat suppression for SPIR (as shown in Figure 6), breaking the log-linearity for both ROIs.

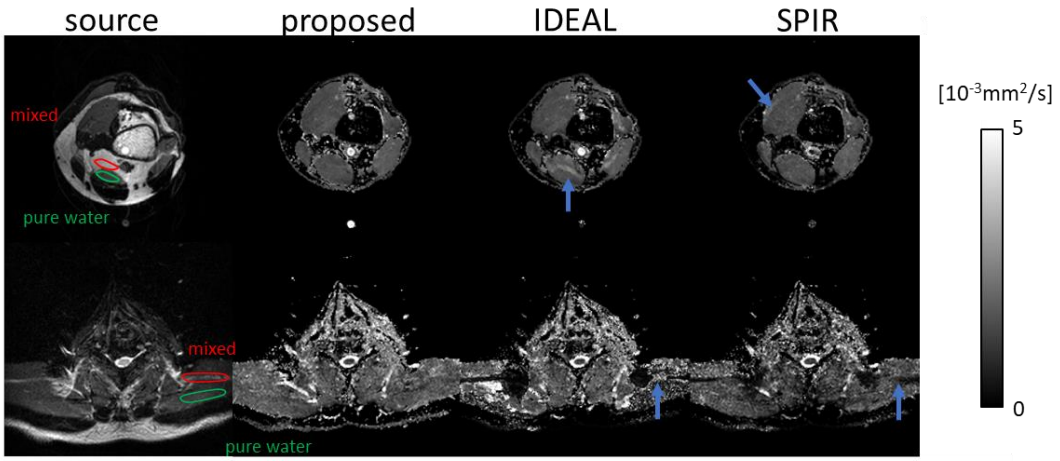

Figure 7. ADC maps of three different approaches in one subject's leg and one subject's shoulder. Source images (non-diffusion) with the corresponding ADC maps are shown, comparing the proposed algorithm, IDEAL, and SPIR. Two ROIs were manually selected in the source images as mixed (water/fat overlap) and pure water (no overlap) regions. In the leg data, IDEAL and SPIR show fat-related artifacts in the mixed region of the ADC map (marked by the blue arrow), which does not appear in the proposed approach's results. For the head-neck region, both IDEAL and SPIR suffer from severe B_0 inhomogeneities, contributing to artifacts in the ADC measurements (marked by blue arrows). In contrast, the proposed algorithm produces smooth ADC maps in the same regions.

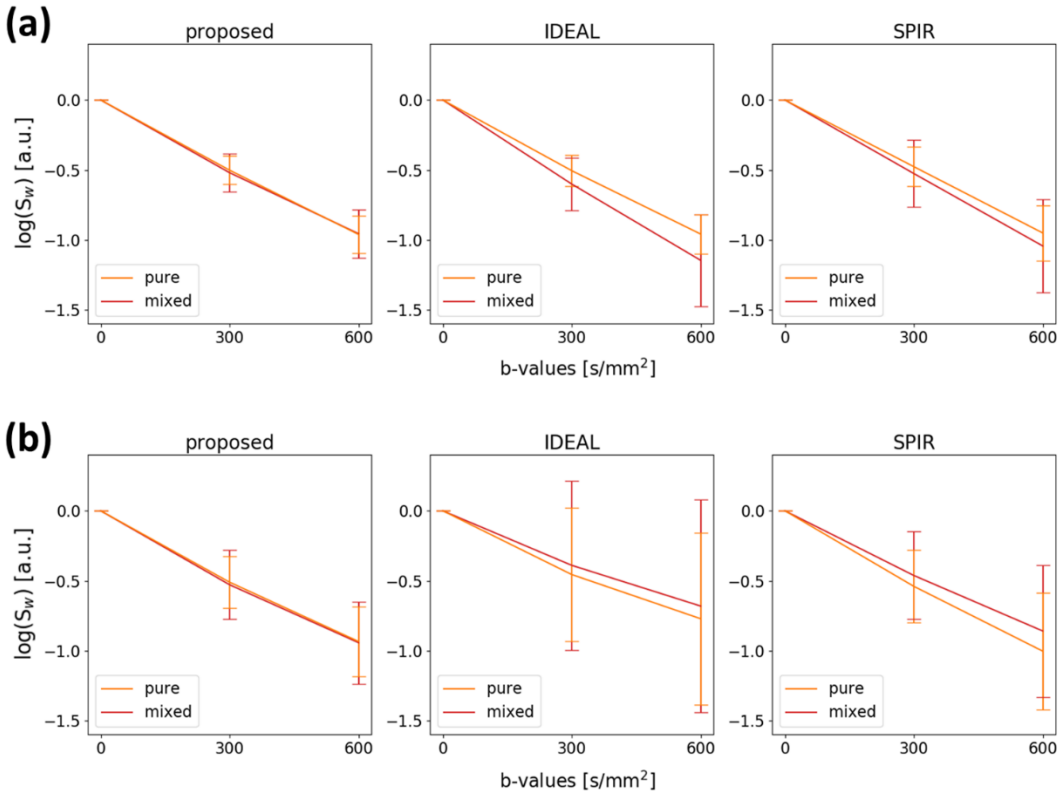

Figure 8. ADC fitting assessment across different volunteers. Natural logarithm plots of average water signal in mixed/pure regions for the leg and the head-neck regions in 6 volunteers (3 volunteers/anatomy) as a function of b-value. For each anatomy, 12 slices (4 slices/volunteer, 3

volunteers) with data in mixed/pure regions are included in the averaging and standard deviation calculations. (a) Leg data. The logarithmic signal decays show reasonable linearity in both ROIs for the proposed method. In contrast, IDEAL shows larger error bars in the mixed regions and significant signal inconsistencies between the two ROIs. SPIR shows a slight difference of logarithmic signal decays between the two ROIs, mainly due to the strong B_1^+ inhomogeneity. (b) Head-neck data. The problematic B_0 inhomogeneity in the head-neck region spoils the log-linearity of the water signal evolution for IDEAL and SPIR in both regions (mixed/pure water). In comparison, the proposed algorithm produces good consistency of the logarithmic signal decays and relatively small deviations in both mixed/pure regions improving ADC fitting consistency.

The improved performance of the proposed algorithm, was also confirmed by calculating the apparent diffusion coefficients. For both anatomies and each technique, the average ADC values, and the P-values from the T-tests between pure/mixed ROIs of water ADC, are displayed in Table 2. The proposed algorithm yields accordant ADC values for the two ROIs with no statistically significant difference between them, whereas IDEAL and SPIR did show significant differences in water ADC between the two ROIs for both anatomies.

Table 2. Quantitative assessment of ADC ($\times 10^{-3}$ mm^2/s) among the three methods

	proposed	**IDEAL**	**SPIR**
Leg			
Mixed	1.62 ± 0.26	1.93 ± 0.49	1.74 ± 0.51
Pure	1.62 ± 0.22	1.61 ± 0.23	1.58 ± 0.32
P-value[a]	0.498	0.001	0.001
Head-neck			
Mixed	1.59 ± 0.45	1.09 ± 1.31	1.44 ± 0.75
Pure	1.58 ± 0.38	1.32 ± 1.03	1.69 ± 0.61
P-value	0.218	0.001	0.001

[a]P-values are derived from group-wise comparison using a paired T-test between ADC values of mixed and pure regions for each technique

2.4 DISCUSSION

In this work, we proposed an alternative water/fat separation algorithm for chemical-shift encoded EPI. This approach is using a multi-peak fat spectrum signal model and a novel regularized algorithm to jointly estimate water, fat and a single B_0 map using chemical-shift encoded EPI data. This algorithm deals with the finite bandwidth problem in the phase-

encoding direction of EPI. The proposed algorithm can remove most of the present fat signals as demonstrated for simulated and in-vivo data. In-vivo validation has been done for interleaved spin-echo EPI and for more challenging interleaved DWI applications. In all measurements the proposed algorithm produced proper water images, even under challenging ΔB_0 conditions. It should be noted that, based on the signal model of Eq. 1, the proposed algorithm is also applicable to other EPI-based approaches.

There are two difficulties for obtaining accurate water/fat separation for EPI: (I) The chemical-shift displacements of individual fat peaks; (II) The field map estimation in regions with severe field inhomogeneities. The proposed algorithm can resolve them and provides water/fat decomposition for both diffusion and non-diffusion cases. Nevertheless, in cases of severe B_0 inhomogeneities, the effects of these two features are hard to distinguish. This is one of the shortcomings of our validation approach. However, in the relatively homogeneous B_0 experiments, e.g., in Figure 2 and in the leg measurements, the benefit of correcting the spatial spectral shifts can be demonstrated independent of B_0 inhomogeneity effects.

For data acquisition, the TE-shifted DW spin-echo msh-EPI sequence was implemented to enable chemical-shift encoding and reduce geometric distortions[4]. It should be noted that, due to the intrinsic properties of EPI, both the acquisition and reconstruction were based on some assumptions. One limitation of the present work is that alternating chemical-shift displacements of fat in the odd and even “echoes” of the EPI train were ignored in the signal model. This issue results in residual ghosting artifacts in the fat images (see Figures 2 and 4). However, those ghosts are chemical-shift encoded, and hence only appear dominantly in the final fat image. Therefore, such artifacts do not noticeably affect the quality of the final water images and the associated ADC measurements.

Another limitation of the proposed image-domain-based algorithm is the integer shift correction of the fat signal for each individual chemical shifted line, applied in the separation procedure. The small error (see Figure 3), can either be mitigated by choosing an appropriate EPI bandwidth during acquisition or by image interpolation during post-processing to realize close-to-integer shifts for the dominant methylene fat peak signal in the image data (see Supporting Information S.2). Such an interpolation step can potentially also be directly included in the shift matrices to avoid increasing the problem size.

An alternative option would be to solve the water/fat separation problem using a k-space-based approach[42-45]. In the approach of ref.[42], the actual k-space sampling time for each point is used in the separation to correct for chemical-shift displacement effects in both the phase- and frequency-encoded directions. However, the B_0 map is still estimated and demodulated in image space, assuming a smooth B_0 field with neglectable differences between neighboring regions. This method and improved similar approaches show great ability in correcting the relatively minor chemical-shift displacements of fat in non-EPI acquisitions[42-43,45]. However, in EPI, the increased chemical-shift displacements in the phase-encoding direction, may not be neglected as in other sequences. One weakness of the present work is that we compare the proposed approach to only one rather basic water/fat separation algorithm. Further comparisons to different approaches assessing the impact of the spatial signal displacement for fat in EPI can be considered as interesting future work. In the work of Honorato et al.[44], both the B_0 estimation and demodulation, as well as water/fat separation, were performed in k-space. Compared to the proposed algorithm, solving the whole problem in k-space would theoretically correct the ghosting in the fat image originating from the alternating chemical-shift in the readout direction. Moreover, it would at the same time correct susceptibility-introduced geometric distortions. However, ref.[44] has only been implemented for 1D spin warp trajectories with already long computation times. A complete 2D solution is pending and would need further investigation, but is expected to be too slow for clinical applications.

The present work is focused on multi-shot EPI acquisitions, which typically have better SNR compared to single-shot EPI based approaches[17-18,22]. Also, due to the increased bandwidth along the phase-encoding direction, msh-EPI shows strongly reduced geometric distortions[3-4]. Unlike the work of Hu et al.[23], in which the geometrical distortions and chemical-shift displacements are corrected by estimating an appropriate k-space kernel including the PSF-dimension, the proposed algorithm only starts the water/fat separation after the three complex source images were reconstructed. This simplification also limits its scope to correct geometric distortions in advance. Nevertheless, the estimated B_0 map could be used to further correct the geometric distortions by established post-processing approaches[46-48] as shown in Supporting Information Figure S.5.

Similar B_0 demodulation methods in k-space[46-50] can also be considered in combination with k-space based water/fat separation[42-43]. The necessary B_0 map can be estimated in the image space through the proposed algorithm in the first place. With the help of regularization and

shift matrices, the main chemical-shift effects in the phase encoding direction have already been corrected, and the estimated smooth B_0 map is more reliable. Therefore, the geometrical distortions and chemical-shift effects in both directions can be addressed well in this full-model-based hybrid approach, and is a step to be explored in future work.

Apart from the acquisition and reconstruction, another potential source of inconsistency is the variability of the fat spectrum, also depending on the actual sequence parameters, such as the sequence type, TE, and TR. In the present work, spin-echo EPI was exclusively used in a small TE range around 60 ms, which is why invariance of the self-calibrated fat spectrum was assumed for all the sequences used. More accurate calibration of the spectrum can be employed, e.g. using single-voxel stimulated echo acquisition mode (STEAM) spectroscopy based pre-calibration[8,10,51] or self-calibration[34] approaches using more echoes.

The DWI application shown in this work is based on the low-resolution navigator phase information delivered for the IRIS reconstruction. This navigator is not chemical-shift encoded and contains some fat signal and related SENSE unfolding errors. To mitigate the latter, an extrapolation of the coil sensitivity map has been applied (described in detail in Supporting Information Figure S.3). Please note that this is only a simple approximation. GRAPPA[52] could also be a potential candidate for mitigation but needs further investigation. The navigator phase information is also slightly compromised by the remaining fat that is spatially shifted. Approaches to entirely suppress the fat signals in the navigator, for example by using gradient reversal approaches[53], should be the subject of future research.

With respect to the DWI application, this study presents a feasibility study for navigated water/fat separated DWI using interleaved EPI. For clinical application, more diffusion orientations should be acquired to produce reliable Trace ADC quantifications. Considering the large number of images acquired in a clinical setting, further improvements to the computational speed are necessary. To achieve higher efficiency, already estimated B_0 maps from any b-value, diffusion orientation, or neighboring slice could serve as a better initialization, which would lead to fewer iterations. Undersampling in the multi-shot and chemical-shift encoding space are promising approaches for future research when SNR is sufficiently high. Other EPI based applications like diffusion tensor imaging (DTI) or intravoxel incoherent motion (IVIM) imaging approaches are also considered for future investigations.

Conclusion

Applying chemical-shift encoding to msh-EPI can significantly improve the fat suppression and image quality of DWI. The proposed algorithm provides a feasible solution for water/fat separation with EPI and has been validated using synthetic data from simulations and acquired data from healthy volunteers. This algorithm can also be applied to other EPI-based works to provide reliable fat-free images.

Acknowledgements

This work is part of the research program HTSM with project number 17104, which is (partly) financed by the Dutch Research Council (NWO).

References

1. Le Bihan D, Mangin J-F, Poupon C, et al. Diffusion tensor imaging: concepts and applications. *JMRI*. 2001;13(4):534–546.

2. Wu W, Miller KL. Image formation in diffusion MRI: A review of recent technical developments: Review of Image Formation in dMRI. *JMRI*. 2017;46(3):646-662.

3. McKinnon GC. Ultrafast interleaved gradient-echo-planar imaging on a standard scanner. *Magn Reson Med.* 1993;30(5):609-616.

4. Jeong H-K, Gore JC, Anderson AW. High-resolution human diffusion tensor imaging using 2-D navigated multishot SENSE EPI at 7 T. *MRM*. 2013;69(3):793-802.

5. Connolly M, Srinivasan A. Diffusion-Weighted Imaging in Head and Neck Cancer: Technique, Limitations, and Applications. *Magn Reson Imaging* Clin N Am. 2018 Feb;26(1):121-133.

6. King, A.D., Mo, F.K.F., Yu, KH. et al. Squamous cell carcinoma of the head and neck: diffusion-weighted MR imaging for prediction and monitoring of treatment response. *Eur Radiol* 20, 2213–2220 (2010).

7. Vandecaveye V, De Keyzer F, Nuyts S, Deraedt K, Dirix P, Hamaekers P, Vander Poorten V, Delaere P, Hermans R. Detection of head and neck squamous cell carcinoma with diffusion weighted MRI after (chemo)radiotherapy: correlation between radiologic and histopathologic findings. *Int J Radiat Oncol Biol Phys.* 2007 Mar 15;67(4):960-71.

8. Hamilton G, Yokoo T, Bydder M, et al. In vivo characterization of the liver fat ^{1}H MR spectrum. *NMR Biomed*. 2011;24(7):784-790.

9. Wokke BH, Bos C, Reijnierse M, van Rijswijk CS, Eggers H, Webb A, Verschuuren JJ, Kan HE. Comparison of dixon and T1-weighted MR methods to assess the degree of fat infiltration in duchenne muscular dystrophy patients. *J Magn Reson Imaging* 2013;38:619–624.

10. Ren J, Dimitrov I, Sherry AD, Malloy CR. Composition of adipose tis- sue and marrow fat in humans by 1H NMR at 7 Tesla. *J Lipid Res* 2008;49:2055–2062.

11. Zee CS, Segall HD, Terk MR, et al. SPIR MRI in spinal diseases. *J Comput Assist Tomogr* 1992;16:356-360.

12. Udayasankar, U.K., Martin, D., Lauenstein, T., Rutherford, R., Galloway, J., Tudorascu, D. and Sitaraman, S.V. (2008), Role of spectral presaturation attenuated inversion-recovery fat-suppressed T2-weighted MR imaging in active inflammatory bowel disease. *J. Magn. Reson. Imaging*, 28: 1133-1140.

13. Wendl CM, Eiglsperger J, Dendl LM, et al. Fat suppression in magnetic resonance imaging of the head and neck region: is the two-point DIXON technique superior to spectral fat suppression. *Br J Radiol*. 2018;91(1085):20170078. d

14. Anzai Y, Lufkin RB, Jabour BA, Hanafee WN. Fat-suppression failure artifacts simulating pathology on frequency-selective fat-suppression MR images of the head and neck. *AJNR Am J Neuroradiol*. 1992 May-Jun;13(3):879-84.

15. Bae YJ, Choi BS, Jeong HK, Sunwoo L, Jung C, Kim JH. Diffusion-Weighted Imaging of the Head and Neck: Influence of Fat-Suppression Technique and Multishot 2D Navigated Interleaved Acquisitions. *AJNR Am J Neuroradiol*. 2018;39(1):145-150.

16. Williams SE, Heemskerk AM, Welch EB, Li K, Damon BM, Park JH. Quantitative effects of inclusion of fat on muscle diffusion tensor MRI measurements. *J Magn Reson Imaging* 2013;38:1292–1297.

17. Hernando D, Karampinos DC, King KF, Haldar JP, Majumdar S, Georgiadis JG, Liang Z-PP. Removal of olefinic fat chemical-shift artifact in diffusion MRI. Magn Reson Med 2011;65:692–701.

18. Burakiewicz, J., Hooijmans, M.T., Webb, A.G., Verschuuren, J.J., Niks, E.H. and Kan, H.E. (2018), Improved olefinic fat suppression in skeletal muscle DTI using a magnitude-based dixon method. *Magn. Reson. Med.*, 79: 152-159.

19. Glover GH, Schneider E. Three-point Dixon technique for true water/fat decomposition with B0 inhomogeneity correction. *Magn Reson Med*. 1991 Apr;18(2):371-83.

20. Reeder SB, Pineda AR, Wen Z, Shimakawa A, Yu H, Brittain JH, Gold GE, Beaulieu CH, Pelc NJ. Iterative decomposition of water and fat with echo asymmetry and least-squares estimation (IDEAL): application with fast spin-echo imaging. *Magn Reson Med*. 2005 Sep;54(3):636-44.

21. Reeder, S. B., Wen, Z., Yu, H., Pineda, A. R., Gold, G. E., Markl, M., & Pelc, N. J. (2004). Multicoil Dixon Chemical Species Separation with an Iterative Least-Squares Estimation Method. *Magnetic Resonance in Medicine*, 51(1), 35–45.

22. Burakiewicz J, Charles-Edwards DG, Goh V, Schaeffter T. Water-fat separation in diffusion-weighted EPI using an IDEAL approach with image navigator. *Magn Reson Med.* 2015 Mar;73(3):964-72.

23. Hu Z, Wang Y, Dong Z, Guo H. Water/fat separation for distortion-free EPI with point spread function encoding. *Magn Reson Med*. 2019;82(1):251-262.

24. McKinnon GC. Ultrafast interleaved gradient-echo-planar imaging on a standard scanner. *Magn Reson Med*. 1993 Nov;30(5):609-16.

25. Hernando, D., Kellman, P., Haldar, J. P., & Liang, Z. P. (2010). Robust water/fat separation in the presence of large field inhomogeneities using a graph cut algorithm. *Magnetic Resonance in Medicine*, 63(1), 79–90.

26. Yu H, Reeder SB, Shimakawa A, Brittain JH, Pelc NJ. Field map estimation with a region growing scheme for iterative 3-point water-fat decomposition. *Magn Reson Med* 2005;54:1032–1039.

27. Landi, Germana & loli piccolomini, Elena & Zama, Fabiana. (2008). A Total Variation-Based Reconstruction Method for Dynamic MRI. *Comput Math Methods Med. 9.* 10.1080/17486700701839039.

28. Koolstra, K. et al. (2019) 'Cartesian MR fingerprinting in the eye at 7T using compressed sensing and matrix completion-based reconstructions', *Magnetic Resonance in Medicine*, 81(4), pp. 2551–2565.

29. Koolstra k, et al. Joint Iterative Image Reconstruction and Field Map Estimation In Low Field MRI. In: *Proceedings of the 27th Annual Meeting of ISMRM*, Montreal, Canada, 2019. Abstract 2445.

30. Lu, W. and Hargreaves, B.A. (2008), Multiresolution field map estimation using golden section search for water-fat separation. *Magn. Reson. Med.*, 60: 236-244.

31. Liu, C., Bammer, R., & Moseley, M. E. (2007). Parallel imaging reconstruction for arbitrary trajectories using k-space sparse matrices (kSPA). *Magnetic Resonance in Medicine*, 58(6), 1171–1181.

32. Hernando, D., Haldar, J. P., Sutton, B. P., Ma, J., Kellman, P., & Liang, Z. P. (2008). Joint estimation of water/fat images and field inhomogeneity map. *Magnetic Resonance in Medicine*, 59(3), 571–580.

33. Hu, H. H. *et al.* (2012) ISMRM workshop on fat-water separation: Insights, applications and progress in MRI, *Magnetic Resonance in Medicine*, 68(2), pp. 378–388.

34. Yu H, Shimakawa A, McKenzie CA, Brodsky E, Brittain JH, Reeder SB. Multiecho water-fat separation and simultaneous R2* estimation with multifrequency fat spectrum modeling. *Magn Reson Med*. 2008;60(5):1122-1134.

35. Bernstein, M.A., Fain, S.B. and Riederer, S.J. (2001), Effect of windowing and zero-filled reconstruction of MRI data on spatial resolution and acquisition strategy. J. *Magn. Reson. Imaging*, 14: 270-280.

36. Pruessmann KP, Weiger M, Scheidegger MB, Boesiger P. SENSE: sensitivity encoding for fast MRI. *MRM*. 1999;42(5):952–962.

37. Bydder M, Larkman DJ, Hajnal JV. Combination of signals from array coils using image-based estimation of coil sensitivity profiles. *Magn Reson Med* 2002;47:539–548.

38. Henkelman RM, Hardy PA, Bishop JE, Poon CS, Plewes DB. Why fat is bright in RARE and fast spin-echo imaging. *J Magn Reson Imaging* 1992; 2: 533-540.

39. Stokes, A.M., Feng, Y., Mitropoulos, T. and Warren, W.S. (2013), Enhanced refocusing of fat signals using optimized multipulse echo sequences. *Magn. Reson. Med.*, 69: 1044-1055.

40. Pokharel SS, Macura KJ, Kamel IR, Zaheer A. Current MR imaging lipid detection techniques for diagnosis of lesions in the abdomen and pelvis. *Radiographics*. 2013 May;33(3):681-702.

41. Delfaut EM, Beltran J, Johnson G, Rousseau J, Marchandise X, Cotten A. Fat suppression in MR imaging: techniques and pitfalls. *Radiographics*. 1999 Mar-Apr;19(2):373-82.

42. Brodsky, E. K., Holmes, J. H., Yu, H., & Reeder, S. B. (2008). Generalized K-space decomposition with chemical-shift correction for non-Cartesian water-fat imaging. *Magnetic Resonance in Medicine*, 59(5), 1151–1164.

43. Berglund, J., Rydén, H., Avventi, E., Norbeck, O., Sprenger, T., & Skare, S. (2020). Fat/water separation in k-space with real-valued estimates and its combination with POCS. *Magnetic Resonance in Medicine*, 83(2), 653–661.

44. Honorato, J.L., Parot, V., Tejos, C., Uribe, S. and Irarrazaval, P. (2012), Chemical species separation with simultaneous estimation of field map and T2* using a k-space formulation. *Magnetic Resonance Medicine*, 68: 400-408.

45. Lu W, Yu H, Shimakawa A, Alley M, Reeder SB, Hargreaves BA. Water-fat separation with bipolar multiecho sequences. *Magn Reson Med*. 2008 Jul;60(1):198-209.

46. Jezzard, P. and Balaban, R.S. (1995), Correction for geometric distortion in echo planar images from B0 field variations. *Magn. Reson. Med.*, 34: 65-73.

47. P. Munger, G. R. Crelier, T. M. Peters and G. B. Pike, "An inverse problem approach to the correction of distortion in EPI images," in *IEEE Transactions on Medical Imaging*, vol. 19, no. 7, pp. 681-689, July 2000

48. Chen NK, Wyrwicz AM. Optimized distortion correction technique for echo planar imaging. *Magn Reson Med*. 2001 Mar;45(3):525-8.

49. Man LC, Pauly JM, Macovski A. Multifrequency interpolation for fast off-resonance correction. *Magn Reson Med*. 1997;37:785–792.

50. Andersson JL, Skare S, Ashburner J. How to correct susceptibility distortions in spin-echo echo-planar images: application to diffusion tensor imaging. *Neuroimage*. 2003 Oct;20(2):870-88.

51. Wang, X., Hernando, D., & Reeder, S. B. (2016). Sensitivity of chemical-shift-encoded fat quantification to calibration of fat MR spectrum. *Magnetic Resonance in Medicine*, 75(2), 845–851.

52. Griswold MA, Jakob PM, Heidemann RM, et al. Generalized autocalibrating partially parallel acquisitions (GRAPPA). *Magn Reson Med* 2002; 47:1202-1210.

53. Gomori JM, Holland GA, Grossman RI, Gefter WB, Lenkinski RE. Fat suppression by section-select gradient reversal on spin-echo MR imaging. *Radiology*. 1988 Aug;168(2):493-5.

54. T. Cover and P. Hart, "Nearest neighbor pattern classification," in *IEEE Transactions on Information Theory*, vol. 13, no. 1, pp. 21-27, January 1967

55. Jin J, Liu F, Weber E, Li Y, Crozier S. An electromagnetic reverse method of coil sensitivity mapping for parallel MRI - theoretical framework. *J Magn Reson*. 2010 Nov;207(1):59-68.

56. Hamilton J, Franson D, Seiberlich N. Recent advances in parallel imaging for MRI. *Progress in Nuclear Magnetic Resonance Spectroscopy*. 2017 Aug;101:71-95.

57. Ma, Y.-J., Liu, W., Tang, X. and Gao, J.-H. (2015), Improved SENSE imaging using accurate coil sensitivity maps generated by a global magnitude-phase fitting method. *Magn. Reson. Med.*, 74: 217-224.

58. Kolahdouzan.M and Shahabi.C . 2004. Voronoi-based K nearest neighbor search for spatial network databases. *In Proceedings of the Thirtieth international conference on Very large data bases - Volume 30 (VLDB '04).* VLDB Endowment, 840–851.